

μ - η^2 : η^2 -Peroxodicopper(II) Complex with a Secondary Diamine Ligand: A Functional Model of Tyrosinase

Liviu M. Mirica,^{†,§} Deanne Jackson Rudd,[†] Michael A. Vance,[†]
Edward I. Solomon,^{*,†} Keith O. Hodgson,^{*,†,‡} Britt Hedman,^{*,‡} and
T. Daniel P. Stack^{*,†}

Contribution from the Department of Chemistry, Stanford University, California 94305, and
Stanford Synchrotron Radiation Laboratory, SLAC, Stanford University, California 94309

Received October 1, 2005; E-mail: stack@stanford.edu

Abstract: The activation of dioxygen (O₂) by Cu(I) complexes is an important process in biological systems and industrial applications. In tyrosinase, a binuclear copper enzyme, a μ - η^2 : η^2 -peroxodicopper(II) species is accepted generally to be the active oxidant. Reported here is the characterization and reactivity of a μ - η^2 : η^2 -peroxodicopper(II) complex synthesized by reacting the Cu(I) complex of the secondary diamine ligand *N,N'*-di-*tert*-butyl-ethylenediamine (DBED), [(DBED)Cu(MeCN)](X) (**1**·X, X = CF₃SO₃⁻, CH₃SO₃⁻, SbF₆⁻, BF₄⁻), with O₂ at 193 K to give [{Cu(DBED)}₂(O₂)](X)₂ (**2**·X₂). The UV-vis and resonance Raman spectroscopic features of **2** vary with the counteranion employed yet are invariant with change of solvent. These results implicate an intimate interaction of the counteranions with the Cu₂O₂ core. Such interactions are supported further by extended X-ray absorption fine structure (EXAFS) analyses of solutions that reveal weak copper-counteranion interactions. The accessibility of the Cu₂O₂ core to exogenous ligands such as these counteranions is manifest further in the reactivity of **2** with externally added substrates. Most notable is the hydroxylation reactivity with phenolates to give catechol and quinone products. Thus the strategy of using simple bidentate ligands at low temperatures provides not only spectroscopic models of tyrosinase but also functional models.

1. Introduction

The importance of the reaction of dioxygen (O₂) with cuprous ions (Cu(I)) in biological^{1–4} and synthetic oxidative processes^{5–10} has prompted significant efforts toward elucidating the structure–reactivity relationship of the nascent copper/dioxygen (Cu/O₂) species,^{11,12} and small synthetic models have proven valuable in this endeavor.^{13,14} Many of these synthetic models are based on the well-characterized binuclear copper protein hemocyanin

(Hc) in which each Cu is ligated by three histidine residues in both the reduced and oxidized form (Figure 1).¹⁵ In an attempt to emulate this natural system, most modeling studies have relied on sterically encumbered, facial-capping tridentate nitrogen ligands, though studies with diamine ligands are now much more prevalent.^{13,14} In oxyhemocyanin (oxyHc) and all structurally characterized model Cu/O₂ intermediates employing such tridentate ligands, one nitrogen atom of each copper coordination sphere is associated weakly and is considered to be positioned along the Jahn–Teller axis of the Cu(II) center (Figure 1). This structural distortion suggests that bidentate nitrogen ligation of each copper should suffice to stabilize Cu/O₂ intermediates, while concurrently allowing greater accessibility of exogenous substrates to the Cu/O₂ core.

Our efforts in this area have focused on studying the Cu/O₂ reactivity with aliphatic diamine ligands, a large class of inexpensive and easily modifiable ligands. The reactivity of the Cu(I) complexes of such amines with O₂ at low temperature in aprotic solvents with weakly coordinating counteranions has led to the characterization of over 20 different bis(μ -oxo)dicopper(III) (O) species.^{16–19}

[†] Department of Chemistry.

[‡] Stanford Synchrotron Radiation Laboratory.

[§] Current address: Department of Chemistry, University of California at Berkeley, Berkeley, California 94720.

- (1) Solomon, E. I.; Baldwin, M. J.; Lowery, M. D. *Chem. Rev.* **1992**, *92*, 521–542.
- (2) Klinman, J. P. *Chem. Rev.* **1996**, *96*, 2541–2562.
- (3) Solomon, E. I.; Sundaram, U. M.; Machonkin, T. E. *Chem. Rev.* **1996**, *96*, 2563–2606.
- (4) Solomon, E. I.; Chen, P.; Metz, M.; Lee, S.-K.; Palmer, A. E. *Angew. Chem., Int. Ed.* **2001**, *40*, 4570–4590.
- (5) Karlin, K. D.; Tyeklar, Z., Eds. *Bioinorganic Chemistry of Copper*; Chapman & Hall: New York, 1993.
- (6) Kitajima, N.; Moro-Oka, Y. *Chem. Rev.* **1994**, *94*, 737–757.
- (7) Ito, M.; Fujisawa, K.; Kitajima, N.; Moro-Oka, Y. In *Oxygenases and Model Systems*; Funabiki, T., Ed.; Kluwer Academic Publishers: Dordrecht, The Netherlands, 1997; pp 345–376.
- (8) Karlin, K. D.; Zuberbühler, A. D. In *Bioinorganic Catalysis*; Reedijk, J., Bouwman, E., Eds.; Marcel Dekker: New York, 1999; pp 469–534.
- (9) Blackman, A. G.; Tolman, W. B. *Struct. Bond.* **2000**, *97*, 179–211.
- (10) Zhang, C. X.; Liang, H.-C.; Humphreys, K. J.; Karlin, K. D. In *Advances in Catalytic Activation of Dioxygen by Metal Complexes*; Simándi, L. I., Ed.; Kluwer: Dordrecht, Boston, London, 2003; Vol. 26, pp 79–121.
- (11) Schindler, S. *Eur. J. Inorg. Chem.* **2000**, 2311–2326.
- (12) Hatcher, L. Q.; Karlin, K. D. *J. Biol. Inorg. Chem.* **2004**, *9*, 669–683.
- (13) Mirica, L. M.; Ottenwaelde, X.; Stack, T. D. P. *Chem. Rev.* **2004**, *104*, 1013–1045.

- (14) Lewis, E. A.; Tolman, W. B. *Chem. Rev.* **2004**, *104*, 1047–1076.
- (15) Magnus, K. A.; Hazes, B.; Ton-That, H.; Bonaventura, C.; Bonaventura, J.; Hol, W. G. J. *Proteins: Struct., Funct., Genet.* **1994**, *19*, 302–309.
- (16) Mahadevan, V.; Hou, Z. G.; Cole, A. P.; Root, D. E.; Lal, T. K.; Solomon, E. I.; Stack, T. D. P. *J. Am. Chem. Soc.* **1997**, *119*, 11996–11997.
- (17) Mahadevan, V.; DuBois, J. L.; Hedman, B.; Hodgson, K. O.; Stack, T. D. P. *J. Am. Chem. Soc.* **1999**, *121*, 5583–5584.
- (18) Stack, T. D. P. *Dalton Trans.* **2003**, *10*, 1881–1889.

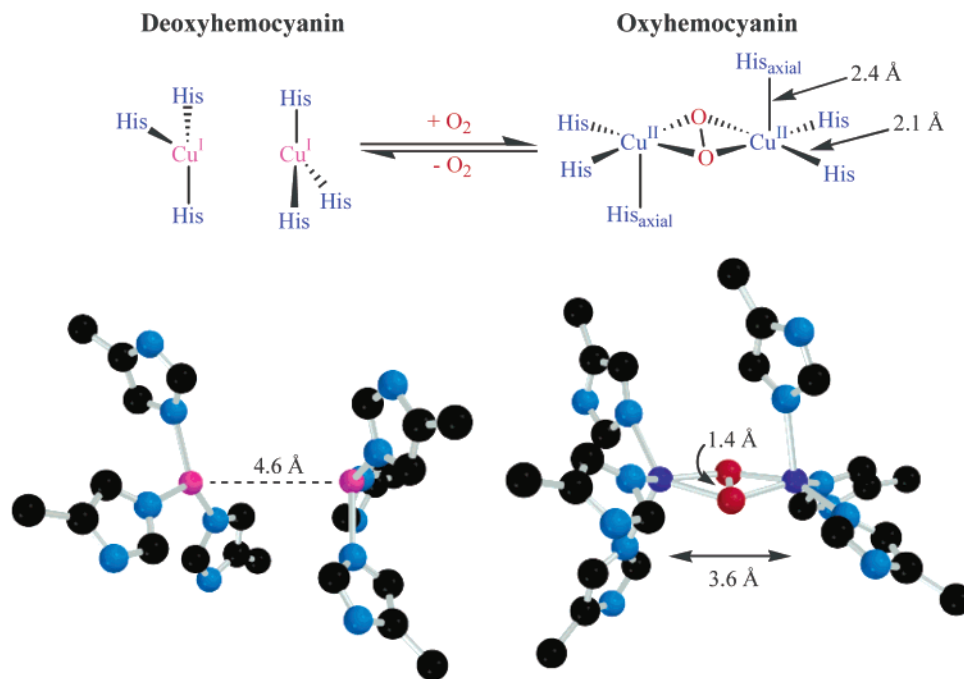


Figure 1. Top: reactivity of hemocyanin with O_2 . Bottom: active site structures of the deoxyHc (left) and oxyHc (right) from *Limulus polyphemus* (horseshoe crab) (ref 15).

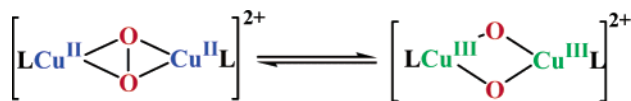


Figure 2. The equilibrium between the **P** and **O** species generated with a neutral ligand **L**.

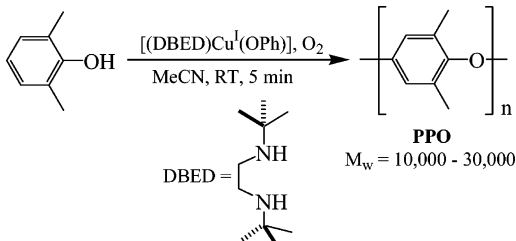


Figure 3. The oxidative polymerization of phenol to PPO by the [(DBED)-Cu(OPh)] complex.

Although most of the Cu(I) complexes of peralkylated diamine ligands (PDLs) react with O_2 to form **O** species,¹⁸ the Cu(I) complexes of a small subset of more sterically demanding ligands react with O_2 to generate an equilibrium mixture of the isoelectronic μ - η^2 : η^2 -peroxidocopper(II) (**P**) and **O** species (Figure 2).²⁰ Defining the ligand attributes and conditions that stabilize each species in these equilibria is an ongoing objective that has been slowed by the dearth of diamine ligands that stabilize a spectroscopically pure **P** species.¹³ Herein is described the thorough characterization of one such system that uses *N,N'*-di-*tert*-butyl-ethylenediamine (DBED, Figure 3), a sterically demanding secondary diamine ligand. This ligand stabilizes a spectroscopically pure **P** species similar to oxyHc and oxytyrosinase (oxyTy).²¹ Interestingly, this new complex exhibits

tyrosinase-like reactivity by hydroxylating phenolates to catechols and quinones, in yields comparable to other reported systems.^{22,23} The reactivity of this **P** species with other substrates has been also investigated and compared with that of the **O** species.²⁴ Beyond the potential biological relevance, interest in the $Cu^I(DBED)/O_2$ reactivity stems from its use in the catalytic oxidative polymerization of phenols to the thermoplastic polyphenylene oxide (PPO, Figure 3).^{25,26}

2. Results and Analysis

2.1. Synthesis and Characterization of [(DBED)Cu(MeCN)]-(X) Complexes. *N,N'*-di-*tert*-butyl-ethylenediamine (DBED) reacts with different Cu(I) salts, $[Cu(MeCN)_4](X)$ ($X = CF_3SO_3^-, CH_3SO_3^-, SbF_6^-, BF_4^-$), in aprotic solvents (THF, CH_2Cl_2 , 2-methyltetrahydrofuran (MeTHF), acetone) under an inert atmosphere to yield light yellow solutions of the Cu(I) complexes [(DBED)Cu(MeCN)](X) (Figure 4, **1·X**).

The **1·X** complexes were generally prepared in situ and used in experiments without isolation or purification. The 1H NMR spectra of **1·CF₃SO₃** reflects an overall C_2 molecular symmetry. If **1·CF₃SO₃** is prepared in situ with $[Cu(MeCN)_4](CF_3SO_3)$, the 1H NMR spectra contains only a single resonance for MeCN at $\delta = 2.05$ ppm, even at 193 K, a chemical shift slightly higher than for MeCN in CD_2Cl_2 . No distinct resonance corresponding to the coordinated MeCN is observed, consistent with a facile exchange of the ligated MeCN with free MeCN on the NMR time scale.

- (19) Cole, A. P.; Mahadevan, V.; Mirica, L. M.; Ottenwaelder, X.; Stack, T. D. P. *Inorg. Chem.* **2005**, *44*, 7345–7364.
 (20) Mahadevan, V.; Henson, M. J.; Solomon, E. I.; Stack, T. D. P. *J. Am. Chem. Soc.* **2000**, *122*, 10249–10250.
 (21) Mirica, L. M.; Vance, M.; Rudd, D. J.; Hedman, B.; Hodgson, K. O.; Solomon, E. I.; Stack, T. D. P. *J. Am. Chem. Soc.* **2002**, *124*, 9332–9333.

- (22) (a) Palavicini, S.; Granata, A.; Monzani, E.; Casella, L. *J. Am. Chem. Soc.* **2005**, *127*, 18031–18036. (b) Santagostini, L.; Gullotti, M.; Monzani, E.; Casella, L.; Dillinger, R.; Tuczak, F. *Chem. Eur. J.* **2000**, *6*, 519–522.
 (23) Itoh, S.; Kumei, H.; Taki, M.; Nagatomo, S.; Kitagawa, T.; Fukuzumi, S. *J. Am. Chem. Soc.* **2001**, *123*, 6708–6709.
 (24) Mirica, L. M.; Vance, M.; Rudd, D. J.; Hedman, B.; Hodgson, K. O.; Solomon, E. I.; Stack, T. D. P. *Science* **2005**, *308*, 1890–1892.
 (25) Aycock, D.; Abolins, V.; White, D. M. In *Encyclopedia of Polymer Science and Engineering*, 2nd ed.; Kroschwitz, J. I., Ed.; John Wiley & Sons: New York, 1986; Vol. 13, p 1.
 (26) Higashimura, H.; Fujisawa, K.; Moro-Oka, Y.; Kubota, M.; Shiga, A.; Terahara, A.; Uyama, H.; Kobayashi, S. *J. Am. Chem. Soc.* **1998**, *120*, 8529–8530.

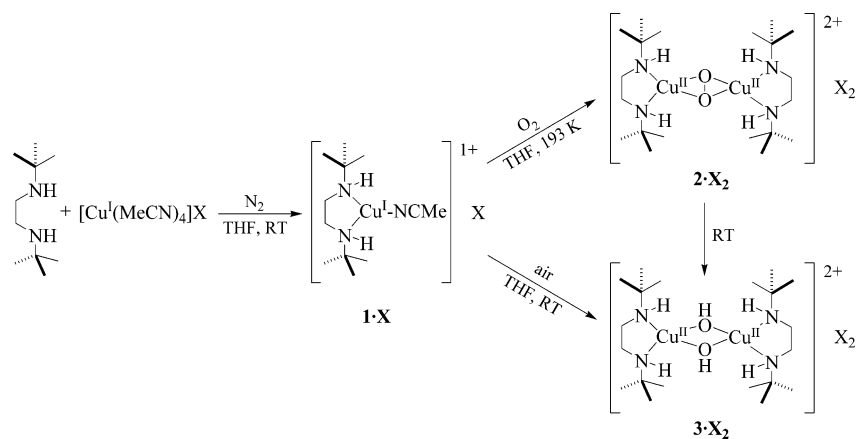


Figure 4. Synthesis of $1\cdot X$, $2\cdot X_2$, and $3\cdot X_2$ ($X = \text{CF}_3\text{SO}_3^-$, CH_3SO_3^- , SbF_6^- , BF_4^-).

Table 1. Crystallographic Data for $1\cdot\text{CF}_3\text{SO}_3$ and $3\cdot(\text{BF}_4)_2$

complex	$1\cdot\text{CF}_3\text{SO}_3$	$3\cdot(\text{BF}_4)_2$
formula	$\text{C}_{13}\text{H}_{27}\text{CuF}_3\text{N}_3\text{O}_3\text{S}$	$\text{C}_{20}\text{H}_{50}\text{Cu}_2\text{B}_2\text{F}_8\text{N}_4\text{O}_2$
MW (g mol^{-1})	425.98	679.34
crystal system	orthorhombic	monoclinic
space group	$Pna2_1$ (no. 33)	$C2/c$ (no. 15)
a (\AA)	12.413(1)	29.989(2)
b (\AA)	15.272(1)	11.697(1)
c (\AA)	10.445(1)	18.921(1)
α (deg)	90.00	90.00
β (deg)	90.00	104.968(1)
γ (deg)	90.00	90.00
volume (\AA^3)	1980.3(1)	6412.0(6)
Z	4	8
T (K)	131 ± 1	184 ± 1
μ (Mo $K\alpha$) (cm^{-1})	12.50	1.40
ρ_{calc} (g cm^{-3})	1.429	1.407
crystal size (mm)	$0.15 \times 0.11 \times 0.04$	$0.29 \times 0.24 \times 0.16$
2θ range	49.4°	52.7°
reflins collected	8844	18266
unique reflections	1762	6507
reflins $F_o^2 > 4\sigma(F_o^2)$	2891	5121
no. of params	245	441
reflins/params ratio	11.80	14.76
R^a	0.037	0.0426
R_w^b	0.096	0.1186

^a $R = \sum||F_o| - |F_c|| / \sum|F_o|$. ^b $R_w = [\sum(w(F_o^2 - F_c^2)^2) / \sum w(F_o^2)^2]^{1/2}$; $w = 1/[\sigma^2(F_o^2) + (0.0784P)^2]$, $P = (F_o^2 + 2F_c^2)/3$.

The X-ray analysis of single crystals of [(DBED)Cu(MeCN)]-(CF_3SO_3) ($1\cdot\text{CF}_3\text{SO}_3$) reveals that the Cu atom is 3-coordinate and is ligated in a trigonal-planar fashion by the DBED ligand and a MeCN molecule (Table 1, Figure 5). The two *tert*-butyl groups are disposed above and below the N_3Cu plane. The $\text{N}-\text{Cu}-\text{N}$ bond angles deviate from the ideal trigonal-planar value of 120° in accord with the $\sim 87^\circ$ acute bite-angle of the DBED ligand. The $\text{Cu}-\text{N}(\text{DBED})$ bond lengths are $\sim 0.03 \text{ \AA}$ shorter than the corresponding bonds in similar tertiary amine Cu(I) complexes.¹⁹ A hydrogen bond exists between one oxygen atom of the triflate counteranion and one $\text{N}-\text{H}$ hydrogen atom ($\text{O}\cdots\text{N} = 3.087 \text{ \AA}$).

2.2. Synthesis of $3\cdot X_2$. At ambient temperatures, the exposure of a solution of $1\cdot X$ ($X = \text{CF}_3\text{SO}_3^-$, BF_4^-) to air rapidly yields [(DBED) $_2\text{Cu}_2(\mu\text{-OH})_2$](X_2) ($3\cdot X_2$, Figure 4), a bis(μ -hydroxy)-dicopper(II) complex, in $>70\%$ yields.²⁷ Such reactivity and yields are typical of other Cu(I)/diamine complexes. X-ray structure analysis of $3\cdot(\text{BF}_4)_2$ reveals a distorted tetrahedral

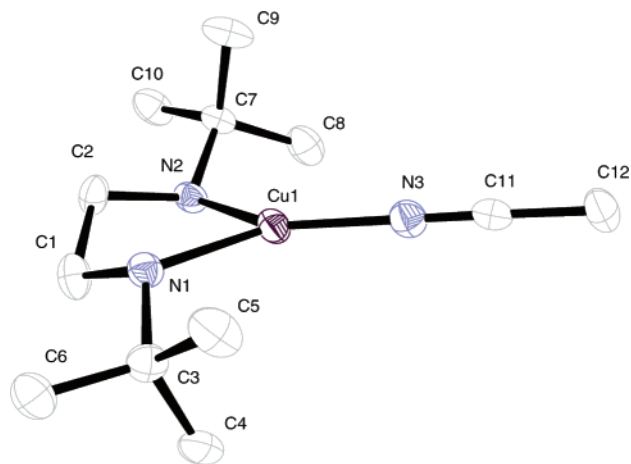


Figure 5. ORTEP representation (50% probability) of the monocation of $1\cdot\text{CF}_3\text{SO}_3$, excluding hydrogen atoms. Selected interatomic distances (\AA) and angles (deg): $\text{Cu}(1)-\text{N}(1)$, 2.054; $\text{Cu}(1)-\text{N}(2)$, 2.043; $\text{Cu}(1)-\text{N}(3)$, 1.863; $\text{N}(3)-\text{C}(11)$, 1.138; $\text{N}(1)\text{Cu}(1)\text{N}(2)$, 87.0 ; $\text{N}(1)\text{Cu}(1)\text{N}(3)$, 135.7 ; $\text{N}(2)\text{Cu}(1)\text{N}(3)$, 137.3 ; $\text{Cu}(1)\text{N}(3)\text{C}(11)$, 178.2 .

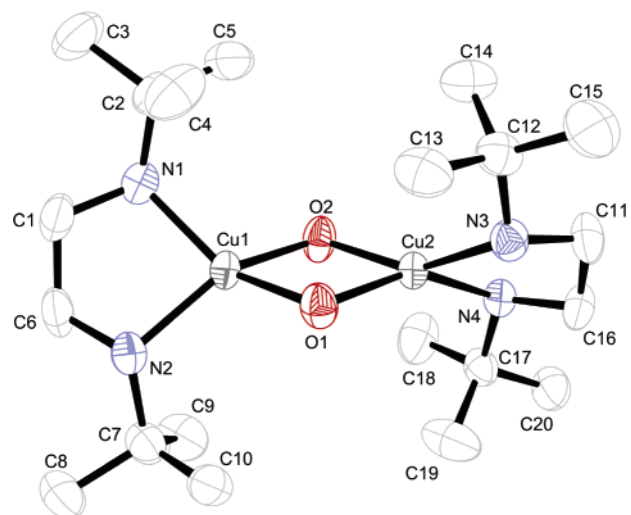


Figure 6. Structure (50% probability) of the dication of $3\cdot(\text{BF}_4)_2$. Selected distances (\AA) and angles (deg) for 3 : $\text{Cu}1\cdots\text{Cu}2$ 2.973, $\text{O}1\cdots\text{O}2$ 2.392, $\text{Cu}-\text{O}_{\text{avg}}$ 1.908, $\text{Cu}-\text{N}_{\text{avg}}$ 2.009, $\text{O}-\text{Cu}-\text{O}_{\text{avg}}$ 77.8 , $\text{Cu}-\text{O}-\text{Cu}_{\text{avg}}$ 101.6 , [plane $\text{N}1-\text{Cu}1-\text{N}2$, plane $\text{N}3-\text{Cu}2-\text{N}4$] 91.2 .

geometry of each copper center (Figure 6, Table 1) with an average twist angle of 46° between the $\text{N}-\text{Cu}-\text{N}$ and $\text{O}-\text{Cu}-\text{O}$ planes.²⁸ Such geometric distortions are uncommon for bis(μ -

(27) Mirica, L. M.; Stack, T. D. P. *Inorg. Chem.* **2005**, *44*, 2131–2133.

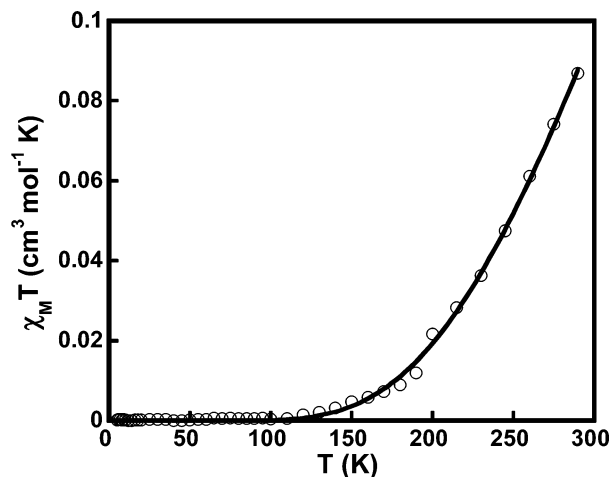


Figure 7. Thermal dependence of $\chi_M T$ for $3 \cdot (\text{CF}_3\text{SO}_3)_2$. The line corresponds to the best theoretical fit with $J = -354 \text{ cm}^{-1}$ and $g = 2.07$.

hydroxy)dicopper(II) complexes. Only one other complex is known with such a large tetrahedral distortion.²⁹ The alternate disposition of the *tert*-butyl groups around the $\text{Cu}_2(\text{OH})_2$ core is consistent with their large steric demands, but the metrical parameters within the $\text{Cu}_2(\text{OH})_2$ core are unexceptional for such dimers (Figure 6). Two F atoms of one BF_4^- counteranion hydrogen bond to an N–H and an O–H group ($\text{F} \cdots \text{N/O} \approx 3.0 \text{ \AA}$). This structure highlights the large steric demands of DBED in Cu(II) dimeric complexes.

2.3. Magnetic Properties of $3 \cdot (\text{CF}_3\text{SO}_3)_2$. Solid-state magnetic measurements of $3 \cdot (\text{CF}_3\text{SO}_3)_2$ are consistent with strong antiferromagnetic coupling between the Cu(II) centers to give a singlet ground state.³⁰ The temperature dependence of the $\chi_M T$ of $3 \cdot (\text{CF}_3\text{SO}_3)_2$ in the temperature range of 5–290 K (Figure 7) shows only a small susceptibility even at room temperature ($\chi_M T = 0.09 \text{ cm}^3 \text{ mol}^{-1} \text{ K}$ at 290 K).²⁷ The molar susceptibility decreases with temperature and becomes negligible below 100 K, as only the singlet ground state is populated at these temperatures. A fit (Figure 7, solid line) of the magnetic data ($\chi_M T$) gives $J = -354 \text{ cm}^{-1}$ and $g = 2.07$ as best-fitted parameters for an analytical expression derived from the Hamiltonian $H = -2J[S_1S_2]$ for local spin values $S = 1/2$: $\chi_M T = (2Ng^2\beta^2/k)[3 + \exp(-2J/kT)]^{-1}$. The g value is typical for a Cu(II) center, and the coupling parameter obtained supports a strong antiferromagnetic interaction.

2.4. Formation of $\mu\text{-}\eta^2\text{:}\eta^2\text{-Peroxodicopper(II) Complexes}$ $[\{\text{Cu}^{\text{II}}(\text{DBED})\}_2(\text{O}_2)](\text{X})_2$. Solutions of $1 \cdot \text{X}$ in aprotic solvents (THF, CH_2Cl_2 , acetone, toluene) react rapidly with O_2 at 193 K to generate thermally sensitive dark green to orange solutions,³¹ the color of which is dependent on the counteranion. The incorporated O_2 could not be displaced reversibly by cycles of evacuation and purging with N_2 , suggesting an irreversible oxidation of the copper centers. These species exhibit characteristically intense absorption bands ($\epsilon = 34\text{--}40 \text{ mM}^{-1} \text{ cm}^{-1}$) at 350–380 nm. Spectroscopic and analytical data support a

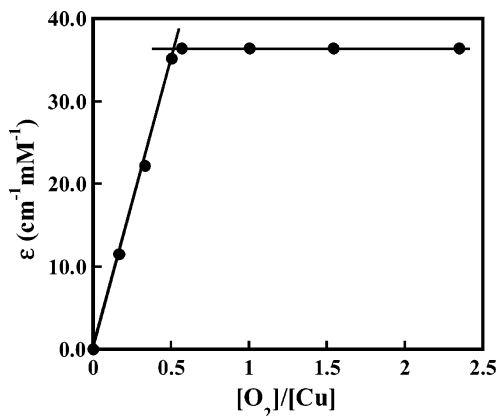


Figure 8. Spectrophotometric titration of a solution of $1 \cdot \text{CF}_3\text{SO}_3$ with O_2 (THF, 193 K, $[\text{Cu}] = 1 \text{ mM}$) under N_2 , as accessed by the absorption at 350 nm.

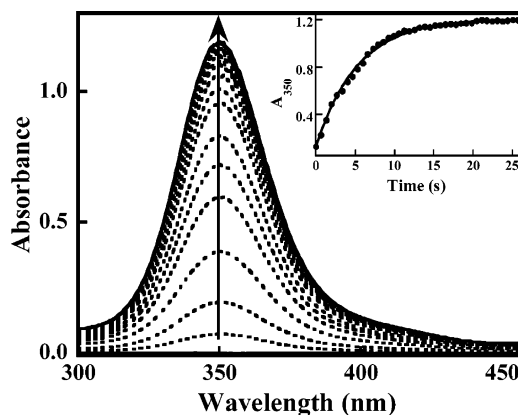


Figure 9. Formation of the $2 \cdot (\text{CF}_3\text{SO}_3)_2$ complex (THF, 193 K, $[\text{O}_2] = 0.3 \text{ mM}$, $[\text{Cu}] = 0.033 \text{ mM}$, $\Delta t = 1.32 \text{ s}$). Inset: fit of the absorbance at 350 nm to a single exponential, $k_{\text{obs}} = 1.9(1) \times 10^{-1} \text{ s}^{-1}$.

$\mu\text{-}\eta^2\text{:}\eta^2\text{-peroxodicopper(II) complex}$ (vide infra), formulated as $[\{\text{Cu}^{\text{II}}(\text{DBED})\}_2(\text{O}_2)](\text{X})_2$ ($2 \cdot \text{X}_2$). The Cu/ O_2 stoichiometry of the oxygenation reaction was determined from optical titrations in which aliquots of dry O_2 were added to a solution of $1 \cdot \text{CF}_3\text{SO}_3$ in THF at 193 K. The concentration of the oxygenated complex was assessed through the increase of the absorbance at 350 nm that does not change after 0.5 equiv of O_2 per copper center is added (Figure 8). This correlates to a Cu/ O_2 ratio of 2:1.1(1).

2.4.1. Formation Kinetics. In general, the oxygenation of Cu(I)/diamine complexes with weakly coordinating counteranions under saturating conditions of O_2 (1 atm) proceeds too rapidly to be followed by standard mixing conditions. Indeed, full formation of $2 \cdot (\text{CF}_3\text{SO}_3)_2$ occurs in less than 5 s (1 atm O_2 , $[\text{O}_2] = 15 \text{ mM}$ in THF,³² $[\text{Cu}] = 0.01\text{--}0.1 \text{ mM}$, 193 K). The observed rate of formation of $2 \cdot (\text{CF}_3\text{SO}_3)_2$ is reduced significantly by saturating the precooled THF solution with a 2% O_2/N_2 gas mixture, providing reaction times longer than 10 s for full formation. Under these conditions, the formation of $2 \cdot (\text{CF}_3\text{SO}_3)_2$ followed by UV–vis spectroscopy is readily fit by a single-exponential process (Figure 9). The rate constant determined is invariant with a change of the initial copper concentration (THF, 193 K, $[\text{Cu}] = 0.01\text{--}0.05 \text{ mM}$). A multiwavelength spectral analysis ($\lambda = 250\text{--}450 \text{ nm}$) gives $k_{\text{obs}} = 1.9(1) \times 10^{-1} \text{ s}^{-1}$ assuming an $\text{A} \rightarrow \text{B}$ model. The observed

(28) DFT broken symmetry geometry optimization in vacuum (B3LYP/6-31G*) converges to the distorted tetrahedral geometry with a twist angle at each copper center of 46° and a Cu–Cu separation of 3.05 Å.

(29) Funahashi, Y.; Nakaya, K.; Hirota, S.; Yamauchi, O. *Chem. Lett.* **2000**, 1172–1173.

(30) Bleaney, B.; Bowers, K. D. *Proc. R. Soc. London, Ser. A* **1952**, 214, 451–465.

(31) The same reaction occurs in MeOH, yet the generated species has a significantly diminished stability.

(32) Cruse, R. W.; Kaderli, S.; Karlin, K. D.; Zuberbühler, A. D. *J. Am. Chem. Soc.* **1988**, 110, 6882–6883.

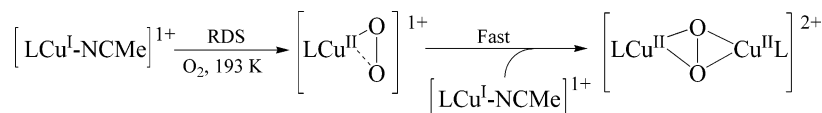


Figure 10. Generally accepted mechanism for the formation of a synthetic $\mu\text{-}\eta^2\text{:}\eta^2\text{-peroxodicopper(II)}$ complex with O_2 , consistent with the reactivity of $1\text{-CF}_3\text{SO}_3$.

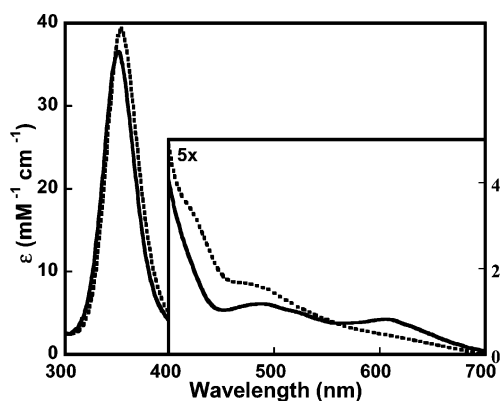


Figure 11. UV-vis spectrum (THF, 193 K, $[\text{Cu}] \approx 1 \text{ mM}$) of $2\text{-(CF}_3\text{SO}_3)_2$ (solid line) and $2\text{-(SbF}_6)_2$ (dashed line). The spectrum of $2\text{-(CH}_3\text{SO}_3)_2$ is identical to that of $2\text{-(CF}_3\text{SO}_3)_2$.

first-order process and the sensitivity of the formation rate on the concentration of O_2 suggests a rate-limiting bimolecular reaction between the Cu(I) complex $1\text{-CF}_3\text{SO}_3$ and O_2 . The observed pseudo-first-order rate constant translates to a second-order rate constant of $6.3(1) \times 10^2 \text{ M}^{-1} \text{ s}^{-1}$, which assumes a linear relationship of dissolved O_2 to the partial pressure of O_2 ($[\text{O}_2] = 0.3 \text{ mM}$). The first-order dependence on the copper concentration and saturation behavior with respect to concentration of O_2 is in agreement with the established reaction mechanism of Cu(I)/amine complexes with O_2 to form **P** complexes (Figure 10).³³ The rate-limiting step during the formation is proposed to be the generation of a Cu(II)–superoxide species that reacts subsequently with a second equiv of the Cu(I) complex to generate the **P** complex. Cu(II)–superoxide accumulation does not occur in this mechanism due to a fast second step.

2.5. Characterization of $\mu\text{-}\eta^2\text{:}\eta^2\text{-Peroxodicopper(II)}$ Complexes, 2-X_2 . **2.5.1. Absorption Spectroscopy.** The absorption spectra of 2-X_2 species (Figure 11) exhibit an exceptionally intense charge-transfer (CT) band ($\sim 350 \text{ nm}$; $\epsilon \approx 34\,000\text{--}40\,000 \text{ M}^{-1} \text{ cm}^{-1}$) and one or two less intense, lower energy bands ($500\text{--}600 \text{ nm}$; $\epsilon \approx 800\text{--}1300 \text{ M}^{-1} \text{ cm}^{-1}$) dependent on the counteranion. The unusually large extinction coefficient of the 350 absorption band was confirmed by a Beer's law plot at 350 nm ($[2\text{-(CF}_3\text{SO}_3)_2] = 0.03\text{--}0.8 \text{ mM}$, THF, 193 K) to give an averaged value for the extinction coefficient of $36\,000 \pm 250 \text{ M}^{-1} \text{ cm}^{-1}$ (Figure S6).³⁴ This value is uncorrected for the $\sim 10\%$ solvent contraction from ambient temperature to 193 K. Variation of the absorption spectra with different counteranions ($\text{X} = \text{CF}_3\text{SO}_3^-, \text{CH}_3\text{SO}_3^-, \text{SbF}_6^-$, Figure 11) suggests an intimate interaction of the counteranions with the Cu_2O_2 core. The unique spectroscopic features of the 2-X_2 species are related directly to the side-on peroxide binding mode of a $\mu\text{-}\eta^2\text{:}\eta^2\text{-}$

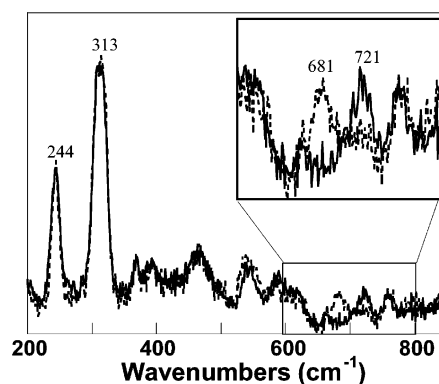


Figure 12. Resonance Raman spectra of $2\text{-(CF}_3\text{SO}_3)_2$ ($\lambda_{\text{ex}} = 351 \text{ nm}$, THF, 77 K, $[\text{Cu}] = 4 \text{ mM}$) with $^{16}\text{O}_2$ (solid line) or $^{18}\text{O}_2$ (dashed line).

peroxodicopper(II) species,¹³ and these characteristic optical features are especially useful for kinetic analyses.

2.5.2. Resonance Raman Spectroscopy. Resonance Raman (rR) spectroscopy is extremely useful for characterizing Cu/ O_2 intermediates. The ability to enhance the intensity of specific vibrational modes by selective excitation into oxygen-based ligand to metal charge-transfer (LMCT) bands provides a direct correlation of the optical features with vibrational modes. In THF, 2-X_2 complexes exhibit a characteristic low-energy O–O stretching vibration at $720\text{--}730 \text{ cm}^{-1}$ on excitation into the LMCT band at $\sim 350 \text{ nm}$, which shifts to lower energy by ca. 40 cm^{-1} with $^{18}\text{O}_2$ (Figure 12). Two isotope insensitive rR features observed at 244 and 313 cm^{-1} are now recognized as Cu–N_{eq} and Cu–Cu stretches, respectively, and their greater intensity compared to that of the ca. 720 cm^{-1} O–O stretching vibration is convenient for identifying **P** species.³⁵ A rR profile analysis of the 350 nm LMCT band unambiguously correlates it with the ca. 300 cm^{-1} vibrational features of **P** isomer; excitations with lower energy laser lines (380, 458, and 496 nm) reveal the decrease in intensity and disappearance of these stretches relative to those of the solvent (Figure 13). As with the absorption spectra, the rR features of the **P** species are sensitive to the choice of counteranion. The three characteristic features at ca. 245, 310, and 720 cm^{-1} vary slightly for $2\text{-(CF}_3\text{SO}_3)_2$, $2\text{-(CH}_3\text{SO}_3)_2$, and $2\text{-(SbF}_6)_2$ (Table 2).

Excitation of solutions of $2\text{-(CF}_3\text{SO}_3)_2$ at 380 or 407 nm gives rise to a weak vibrational feature at 605 cm^{-1} (580 cm^{-1} with $^{18}\text{O}_2$ substitution) that is characteristic of a bis($\mu\text{-oxo}$)dicopper(III) (**O**) complex. This 605 cm^{-1} vibration does not appear with 350 nm excitation, fully consistent with the known absorption features of an **O** species. Calibration of the intensity with known **O** complexes estimates the concentration of the **O** isomer at less than 5% (Figure S7).³⁴

2.5.3. X-ray Absorption Spectroscopy. Structural information of 2-X_2 from single-crystal X-ray crystallography has been elusive in part due to its thermal sensitivity. Cu K-edge X-ray

(33) Karlin, K. D.; Kaderli, K.; Zuberbühler, A. D. *Acc. Chem. Res.* **1997**, *30*, 139–147.

(34) See the Supporting Information.

(35) Henson, M. J.; Mahadevan, V.; Stack, T. D. P.; Solomon, E. I. *Inorg. Chem.* **2001**, *40*, 5068–5069.

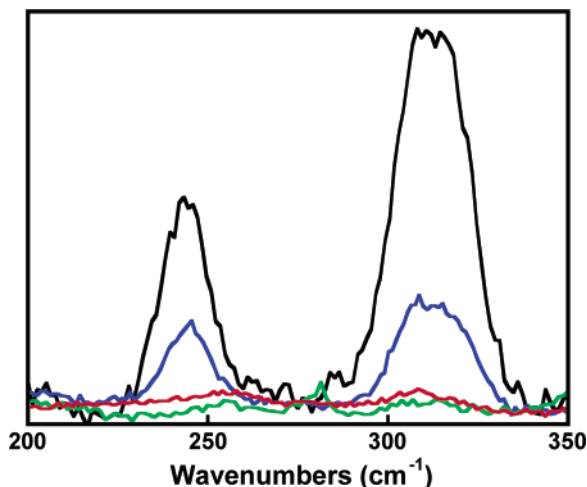


Figure 13. rR excitation profile of the two low energy rR features of $2\cdot(\text{CF}_3\text{SO}_3)_2$ at 351 (black), 380 (blue), 458 (green), and 496 nm (red) (THF, 77 K, $[\text{Cu}] = 4$ mM). Spectra were scaled to the ca. 880 cm^{-1} feature of THF.

Table 2. UV–Vis and rR Spectroscopic Features of $2\cdot\text{X}_2$ in THF

complex	UV–vis features	rR features
	λ , nm (ϵ , $\text{mM}^{-1}\text{ cm}^{-1}$)	ν , cm^{-1} ($\Delta^{18}\text{O}_2$, cm^{-1})
$2\cdot(\text{CF}_3\text{SO}_3)_2$	350 (36)	244 (0)
	485 (1.2)	313 (0)
	605 (0.9)	724 (40)
$2\cdot(\text{CH}_3\text{SO}_3)_2$	349 (36)	245 (0)
	485 (1.1)	312 (0)
	604 (0.9)	720 (40)
$2\cdot(\text{SbF}_6)_2$	353 (38)	241 (0)
	425 (1.7)	308 (0)
	472 (2.1)	725 (40)

absorption spectroscopy (XAS) of solutions of $2\cdot\text{X}_2$, however, provides key insights into its structure and oxidation state description.

A preedge feature at 8979.5 eV for all $2\cdot\text{X}_2$ complexes is consistent with a Cu(II) oxidation state description (Figure 14).³⁶ The extended X-ray absorption fine structure (EXAFS) analysis of $2\cdot(\text{CF}_3\text{SO}_3)_2$ clearly requires a $\text{Cu}\cdots\text{Cu}$ contribution at a distance of 3.45 Å, a distance similar to other structurally characterized **P** complexes;^{37–39} each Cu is best fit as a 5- rather than 4-coordinate center with four N/O⁴⁰ ligands at 1.96 Å and an additional O/N ligand at 2.53 Å (Figure 15, top). The latter distance is consistent with an axially bound oxygen atom from a weakly associated CF_3SO_3^- counteranion (Table 3).¹⁷

The variation of the UV–vis and rR spectra with a change in the counteranion and not the solvent suggests an intimate interaction of the anions with the cationic complex, which is supported by the EXAFS experiments. $2\cdot(\text{CH}_3\text{SO}_3)_2$ and

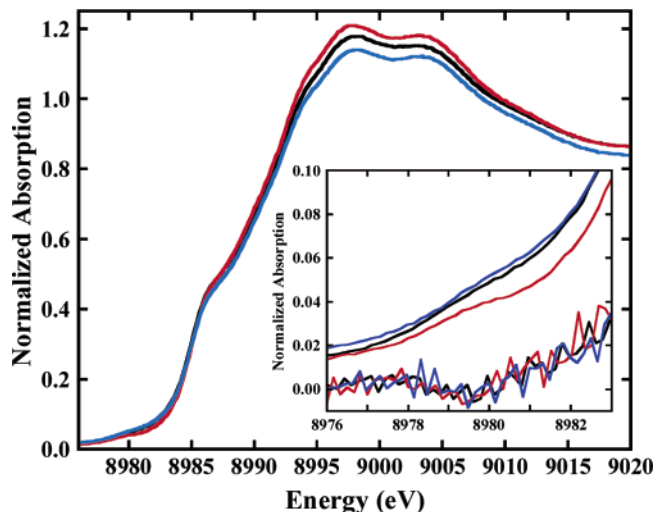


Figure 14. Cu K-edge absorption spectrum of $2\cdot(\text{CF}_3\text{SO}_3)_2$ (red), $2\cdot(\text{CH}_3\text{SO}_3)_2$ (black), and $2\cdot(\text{SbF}_6)_2$ (blue) in THF (10 K, $[\text{Cu}] = 2$ mM). Inset: amplified view of $1s \rightarrow 3d$ preedge transition areas and their second derivatives showing the low-intensity transition at 8979.5 eV typical for Cu(II) (ref 36).

Table 3. EXAFS Fit Results for $2\cdot\text{X}_2^a$

complex	fit		R (Å)	σ^2 (Å ²)	ΔE_0	F^b				
$2\cdot(\text{CF}_3\text{SO}_3)_2$	1	4 O/N ^c	1.96	0.0051	−6.24	0.22				
		2 C	2.84	0.0022						
		1 Cu	3.45	0.0079						
	2	4 O/N ^c	1.96	0.0052	−7.14	0.17				
		1 O	2.53	0.0066						
		2 C	2.83	0.0020						
		1 Cu	3.45	0.0075						
		$2\cdot(\text{CH}_3\text{SO}_3)_2$	1	4 O/N ^c			1.93	0.0071	−9.57	0.26
				2 C			2.81	0.0083		
1 Cu	3.45			0.0087						
2	4 O/N ^c		1.94	0.0070	−7.61	0.11				
	1 O		2.24	0.0094						
$2\cdot(\text{SbF}_6)_2$	1	4 O/N ^c	1.98	0.0080	−7.50	0.51				
		1 F/O ^c	2.53	0.0027						
		4 C	2.84	0.0078						
		1 Cu	3.49	0.0059						
		8 C–N	4.08	0.0085						
		2	2 O/N ^c	1.85			0.0057	−10.89	0.35	
	2 N/O ^c		1.99	0.0009						
	4 C		2.74	0.0334						
	3	2 O/N ^c	1.85	0.0069	−10.23	0.29				
2 N/O ^c		1.99	0.0014							
1 F/O ^c		2.53	0.0037							
4 C		2.83	0.0099							
		1 Cu	3.47	0.0066						

^a Errors are estimated to be 25% for coordination numbers and 0.01–0.03 Å for distances. ^b Error (F) is defined as $F = [\sum k^6(\chi_{\text{obsd}} - \chi_{\text{calcd}})^2]/n$, where n is the number of data points. ^c Scatterers differing by $Z = \pm 1$ are not distinguishable by EXAFS. The ordering O/N indicates that an oxygen atom was used to model the backscattering in the fit.

$2\cdot(\text{SbF}_6)_2$ have a more and less coordinating counteranion, respectively, than $2\cdot(\text{CF}_3\text{SO}_3)_2$. The best EXAFS fit for $2\cdot(\text{CH}_3\text{SO}_3)_2$ requires a $\text{Cu}\cdots\text{Cu}$ contribution (3.45 Å), and 5-coordinate Cu center with four N/O ligands at 1.96 Å and an additional ligand at ~ 2.24 Å, consistent with an axially bound oxygen atom from a CH_3SO_3^- counteranion (Figure 15, middle,

(36) Kau, L.-S.; Spira-Solomon, D. J.; Penner-Hahn, J. E.; Hodgson, K. O.; Solomon, E. I. *J. Am. Chem. Soc.* **1987**, *109*, 6433–6442.

(37) Kitajima, N.; Fujisawa, K.; Fujimoto, C.; Moro-Oka, Y.; Hashimoto, S.; Kitagawa, T.; Toriumi, K.; Tatsumi, K.; Nakamura, A. *J. Am. Chem. Soc.* **1992**, *114*, 1277–1291.

(38) Koder, M.; Katayama, K.; Tachi, Y.; Kano, K.; Hirota, S.; Fujinami, S.; Suzuki, M. *J. Am. Chem. Soc.* **1999**, *121*, 11006–11007.

(39) Hu, Z. B.; Williams, R. D.; Tran, D.; Spiro, T. G.; Gorun, S. M. *J. Am. Chem. Soc.* **2000**, *122*, 3556–3557.

(40) EXAFS analysis typically cannot distinguish between atoms that differ in Z by 1 (e.g., O and N) (Scott, R. A. *Methods Enzymol.* **1985**, *117*, 414). Given the k range of the EXAFS data ($k = 3\text{--}12.5\text{ \AA}^{-1}$), any difference in R less than 0.17 Å between ligands in the first coordination shell (at 1.89 Å) could not be resolved. However, for $2\cdot(\text{SbF}_6)_2$ it was possible to separate the first coordination shell into two distinct scattering shells.

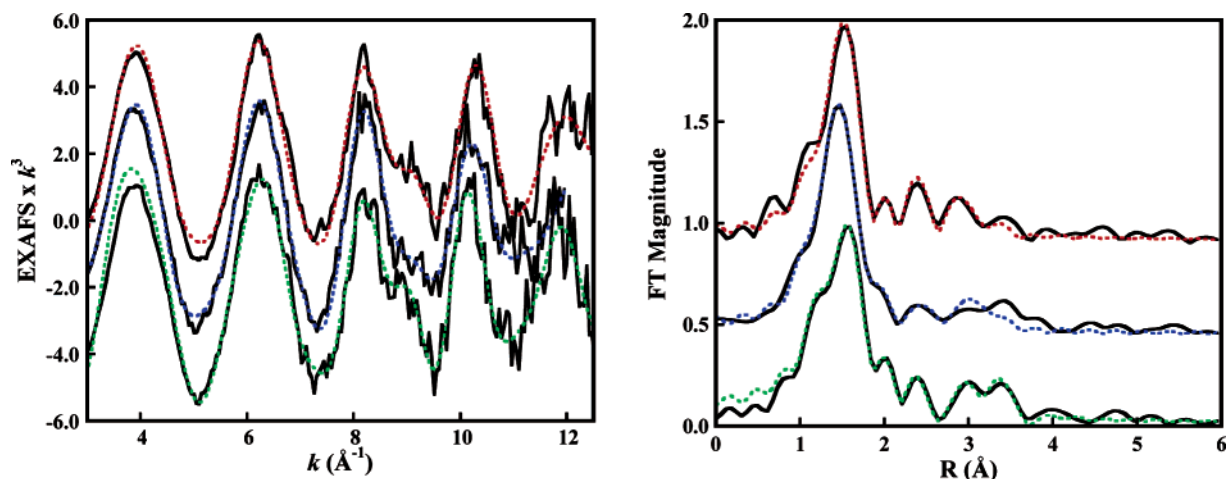


Figure 15. EXAFS data (left, solid lines) and nonphase shift corrected FT (right, solid lines) of $2\cdot(\text{CF}_3\text{SO}_3)_2$, $2\cdot(\text{CH}_3\text{SO}_3)_2$, and $2\cdot(\text{SbF}_6)_2$ from top to bottom, and best fits (dashed lines) from Table 3.

and Table 3). This postulated $\text{CH}_3\text{SO}_3^-/\text{Cu}$ interaction is shorter than that for CF_3SO_3^- in $2\cdot(\text{CF}_3\text{SO}_3)_2$ (2.24 Å vs 2.53 Å, respectively) as would be anticipated for a more basic counteranion.

While the EXAFS spectra of $2\cdot(\text{CF}_3\text{SO}_3)_2$ and $2\cdot(\text{CH}_3\text{SO}_3)_2$ are similar, the EXAFS spectrum of $2\cdot(\text{SbF}_6)_2$ is discernibly different. The fit of the Fourier transform (FT) of $2\cdot(\text{SbF}_6)_2$ allowed a splitting of the first shell of scatterers into 2 O/N and 2 N/O atoms at 1.85 and 1.99 Å, respectively. As in the other samples, an additional F/O atom ligand is needed at 2.53 Å (Figure 15, bottom, and Table 3) for a good fit to the data.⁴¹

2.5.4. Theoretical Characterization of 2. Complex **2** was investigated by density functional theory (DFT) methods. On the basis of previous studies, hybrid DFT methods (B3LYP)^{42,43} best reproduce the metrical parameters available from crystal structures of related synthetic complexes and EXAFS analyses of **2**. A localized solution for the singlet ground-state wave function of the **P** species is obtained using the broken symmetry formalism.⁴⁴ For this study, the B3LYP/6-31G* method provides remarkably good correlations to the metrical parameters at minimal computational cost. While a double- ζ basis set may not provide appropriate total energy estimates, it has been widely employed for geometry optimization calculations. Selected calculated metrical parameters and a space-filling model of the calculated structure of **2** are shown in Figure 16.

2.6. Decomposition Kinetics. Though examples of synthetic **P** species that are stable at ambient temperatures exist,³⁸ most **P** species are generally stable only at low temperatures and decompose upon warming primarily by processes involving ligand oxidation.¹⁴ The kinetics of thermal decomposition of $2\cdot\text{X}_2$ were studied by UV-vis spectroscopy and multiwavelength spectral analysis. As the rate of thermal decay is not altered significantly by counteranion choice, the following kinetic studies focused on $2\cdot(\text{CF}_3\text{SO}_3)_2$. This complex is remarkably stable at 193 K ($t_{1/2} \approx 20$ days), yet decomposes at elevated temperatures. The time-dependent evolution of the

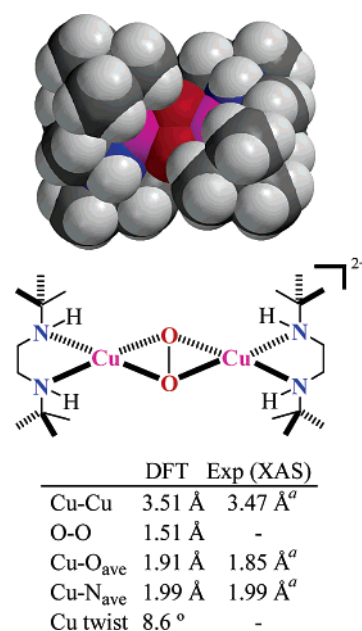


Figure 16. Calculated and experimental metrical parameters for **2**. “a” indicates that these parameters are from the $2\cdot(\text{SbF}_6)_2$ EXAFS data.

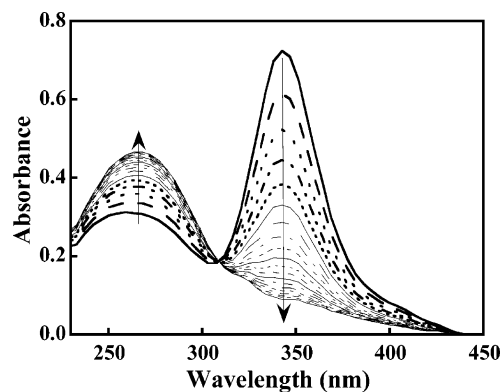


Figure 17. Typical thermal decay of $2\cdot(\text{CF}_3\text{SO}_3)_2$ (THF, 258 K, $[\text{Cu}] = 0.4$ mM, 0.1 cm path length, $\Delta t = 50$ s).

absorbance profile ($\lambda = 250\text{--}450$ nm) was successfully fitted in each case to a first-order $\text{A} \rightarrow \text{B}$ model involving two principal colored components (Figure 17). The measured rate constants of decay are invariant to Cu concentrations ($[\text{Cu}] =$

(41) Oxygen/nitrogen and oxygen/fluorine scatterers cannot be distinguished in an EXAFS fit.

(42) Metz, M.; Solomon, E. I. *J. Am. Chem. Soc.* **2001**, *123*, 4938–4950.

(43) Szilagy, R. K.; Metz, M.; Solomon, E. I. *J. Phys. Chem. A* **2002**, *106*, 2994–3007.

(44) Li, J.; Noodleman, L.; Case, D. A. In *Inorganic Electronic Structure and Spectroscopy*; Solomon, E. I., Lever, A. B. P., Eds.; John Wiley & Sons: New York, 1999; Vol. 1, pp 661–724.

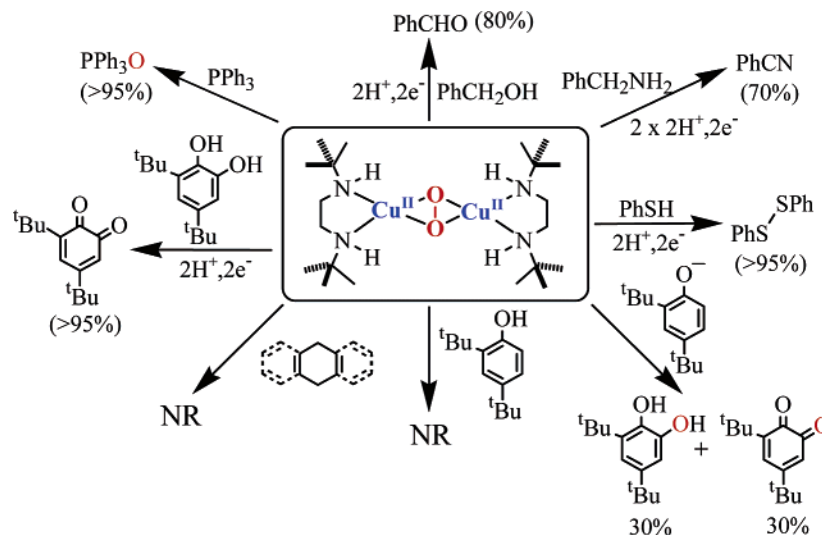


Figure 18. Reactivity of $2\cdot(\text{CF}_3\text{SO}_3)_2$ toward exogenous substrates (NR: no reaction; general conditions: N_2 , THF, 1–2 equiv of substrate, 193 K, $[\text{Cu}] = 2 \text{ mM}$).

0.1–1.5 mM), supporting a first-order dependence on the complex. An Eyring analysis of this decomposition in THF (195–271 K) gives activation parameters of $\Delta H^\ddagger = 14.8 \pm 0.5 \text{ kcal mol}^{-1}$ and $\Delta S^\ddagger = 10 \pm 1 \text{ cal mol}^{-1} \text{ K}^{-1}$.³⁴ Deuteration of the N–H groups does not alter the thermal decay rate in THF at 233 K, indicating that the rate-determining step does not involve N–H bond cleavage.

2.7. Reactivity with Exogenous Substrates. Thermal decay of $2\cdot(\text{CF}_3\text{SO}_3)_2$ in the absence of any added substrate leads to a bis(hydroxy)dicopper(II) complex, $3\cdot(\text{CF}_3\text{SO}_3)_2$ as the major product (>70% yield), similar to other Cu/O_2 species.⁴⁵ In contrast to the thermal decay at higher temperatures, the stability of $2\cdot(\text{CF}_3\text{SO}_3)_2$ at 173 K allows the reactivity with exogenous substrates to be examined. $2\cdot(\text{CF}_3\text{SO}_3)_2$ reacts rapidly with PPh_3 , 2,4-di-*tert*-butylcatechol, or thiophenol to give PPh_3O , 2,4-di-*tert*-butylquinone, or phenyl disulfide, respectively. On the basis of the oxidizing equivalents of **2**, the yields were greater than 95%. $2\cdot(\text{CF}_3\text{SO}_3)_2$ also reacts with benzyl alcohol and benzylamine to give good yields of benzaldehyde (80%) and benzonitrile (70%), respectively (Figure 18). However, $2\cdot(\text{CF}_3\text{SO}_3)_2$ showed no apparent reactivity (<5% yield) toward large excesses of 1,4-cyclohexadiene, 9,10-dihydroanthracene, or 2,4-di-*tert*-butylphenol at 193 K for 6 h.

Most notable is the tyrosinase-like reactivity of $2\cdot(\text{CF}_3\text{SO}_3)_2$ with 1–2 equiv of sodium or lithium salts of 2,4-di-*tert*-butylphenol at 193 K under N_2 . Upon acidic workup, a ca. 1:1 mixture of 3,5-di-*tert*-butylcatechol and 3,5-di-*tert*-butyl-1,2-benzoquinone are found as products (Figure 18), accounting for ~90% of the oxidizing equivalents of $2\cdot(\text{CF}_3\text{SO}_3)_2$. This yield assumes that 2 equiv of $2\cdot(\text{CF}_3\text{SO}_3)_2$ are needed for formation of 1 equiv of quinone from phenolate with no reduction of the $\text{Cu}(\text{II})$ centers. The formation of $2\cdot(\text{CF}_3\text{SO}_3)_2$ with $^{18}\text{O}_2$ followed by reaction with 2,4-di-*tert*-butylphenolate yields catechol and quinone products containing a single labeled oxygen atom (>80% ^{18}O atom incorporation), as assessed by ESI-MS.³⁴

3. Discussion

The formation and stabilization of a $\mu\text{-}\eta^2\text{:}\eta^2\text{-peroxodicopper(II)}$ (**P**) complex with DBED, a aliphatic diamine ligand, is

intriguing not only because it is a secondary diamine in an ostensibly oxidizing environment,^{21,46} but also because the majority of peralkylated diamine ligands (PDLs) are known to react with $\text{Cu}(\text{I})$ and O_2 to generate bis($\mu\text{-oxo}$)dicopper(III) (**O**) complexes.¹⁶ Some $\text{Cu}(\text{I})/\text{PDLs}$ complexes form measurable mixtures of the isomeric **P** and **O** species,²⁰ but it is generally accepted that PDLs preferentially stabilize **O** species. Escalating the steric demands of the ligand destabilizes the more compact **O** species through intraligand and ligand/ Cu_2O_2 core steric interactions thereby biasing the equilibrium to the **P** isomer, which possesses a significantly longer $\text{Cu}\cdots\text{Cu}$ separation (ca. 3.5 Å for **P** vs ca. 2.8 Å for **O**).¹³

The reaction of DBED with $\text{Cu}(\text{I})$ salts yields a trigonal $\text{Cu}(\text{I})$ complex with an exogenous MeCN ligand, $[(\text{DBED})\text{-Cu}(\text{MeCN})](\text{X})$ ($\text{X} = \text{CF}_3\text{SO}_3^-, \text{CH}_3\text{SO}_3^-, \text{SbF}_6^-, \text{BF}_4^-, \mathbf{1}\cdot\text{X}$). These $\text{Cu}(\text{I})$ complexes react with O_2 at room temperature to yield bis($\mu\text{-hydroxy}$)dicopper(II) complexes $[(\text{DBED})_2\text{Cu}_2(\mu\text{-OH})_2](\text{X})_2$ ($\mathbf{3}\cdot\text{X}_2$) and at 193 K to generate thermally sensitive $\mu\text{-}\eta^2\text{:}\eta^2\text{-peroxodicopper(II)}$ complexes $\{[\text{Cu}(\text{DBED})]_2(\text{O}_2)\}(\text{X})_2$ ($\mathbf{2}\cdot\text{X}_2$). These complexes are EPR silent and NMR active due to the strong antiferromagnetic coupling between the two $S = 1/2$ $\text{Cu}(\text{II})$ centers. The UV–vis spectra of $\mathbf{2}\cdot\text{X}_2$ complexes in THF exhibit characteristic oxygen-based LMCT absorptions (Figure 11),^{37,38,47} except that the extinction coefficient of the 350 nm feature is exceptionally large ($\epsilon = 36 \text{ mM}^{-1} \text{ cm}^{-1}$) compared to those of other **P** species ($\epsilon = 24 \text{ mM}^{-1} \text{ cm}^{-1}$).¹³ On the basis of extensive spectroscopic and theoretical studies, the UV–vis absorption features have been assigned as in-plane $\pi_\sigma^* \rightarrow d_{xy}$ and out-of-plane $\pi_\nu^* \rightarrow d_{xy}$ peroxo to $\text{Cu}(\text{II})$ CT transitions for the ca. 350 and 530 nm absorption bands, respectively.^{4,48–50} The in-plane $\pi_\sigma^* \rightarrow d_{xy}$ feature is more intense, reflecting better orbital overlap than the out-of-plane

(45) Upon thermal decomposition of $2\cdot(\text{CF}_3\text{SO}_3)_2$, only about 80% of the unoxidized ligand was recovered.

(46) Komiyama, K.; Furutachi, H.; Nagatomo, S.; Hashimoto, A.; Hayashi, H.; Fujinami, S.; Suzuki, M.; Kitagawa, T. *Bull. Chem. Soc. Jpn.* **2004**, *77*, 59–72.

(47) Cahoy, J.; Holland, P. L.; Tolman, W. B. *Inorg. Chem.* **1999**, *38*, 2161–2168.

(48) Ross, P. K.; Solomon, E. I. *J. Am. Chem. Soc.* **1990**, *112*, 5871–5872.

(49) Ross, P. K.; Solomon, E. I. *J. Am. Chem. Soc.* **1991**, *113*, 3246–3259.

(50) Solomon, E. I.; Tuzcek, F.; Root, D. E.; Brown, C. A. *Chem. Rev.* **1994**, *94*, 827–856.

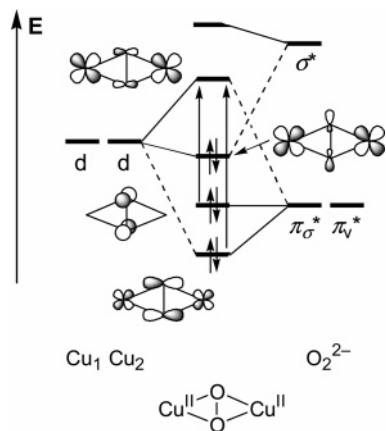


Figure 19. Approximate MO diagrams for the $\mu\text{-}\eta^2\text{:}\eta^2\text{-peroxodicopper(II)}$ complex. The arrows represent the assignment of the two peroxide to metal charge-transfer transitions.

$\pi_v^* \rightarrow d_{xy}$ feature (Figure 19). For $2\cdot(\text{CF}_3\text{SO}_3)_2$, the higher intensity of the 350 nm band, confirmed by oscillator strengths comparison among several **P** species,⁵¹ suggests a greater donor interaction between the Cu and peroxide orbitals.

rR spectroscopy of $2\cdot(\text{CF}_3\text{SO}_3)_2$ in THF also confirms a **P** structure⁵² with a low vibration $\nu_{\text{O-O}} = 721 \text{ cm}^{-1}$ ($\Delta(^{18}\text{O}_2) = 40 \text{ cm}^{-1}$). The lower O–O stretching frequency compared to that of a typical peroxide ion (ca. 850 cm^{-1}) is thought to result from back-bonding by the Cu(II) centers into the σ^* orbital of the peroxide ion (Figure 19).⁵³ This back-bonding weakens the O–O bond and provides a potential pathway by which the O–O bond can be cleaved. The lower energy of the O–O vibration for $2\cdot(\text{CF}_3\text{SO}_3)_2$ as compared to those of other characterized **P** species further supports a stronger donor interaction between the Cu and peroxide orbitals and the associated increased back-donation from the Cu(II) centers. The rR spectra also reveal two oxygen-isotope insensitive vibrations at ~ 244 and $\sim 313 \text{ cm}^{-1}$ (Figure 12, Table 2) that are assigned as Cu–N_{eq} and Cu–Cu stretches, respectively.³⁵ Comparative values of 322 and 296 cm^{-1} are found for the **P** species generated with *N,N'*-di-*tert*-butyl-*N,N'*-di-methyl-ethylenediamine (DBDMED), a closely related ligand. The ligand variation from DBED to DBDMED leads to an energy increase in the Cu–N_{eq} vibration and an energy decrease in the Cu–Cu vibration. Both trends are in accord with weaker donation of secondary amines in these **P** species that correspondingly leads to stronger bonding interactions within the Cu₂O₂ core and thus a more intense $\pi_{\sigma}^* \rightarrow d_{xy}$ LMCT transition (vide supra).

The thermal instability of **2** has precluded any X-ray crystallographic analysis, yet critical oxidation state assignments and metrical parameters are accessible through solution Cu K-edge X-ray absorption spectroscopy (XAS). All samples of $2\cdot\text{X}_2$ exhibit a preedge feature at 8979.5 eV, consistent with a Cu(II) complex (Figure 14).³⁶ The EXAFS analysis of each complex gives a Cu···Cu distance of ca. 3.46 Å that is effectively invariant with the EXAFS model. While short, this

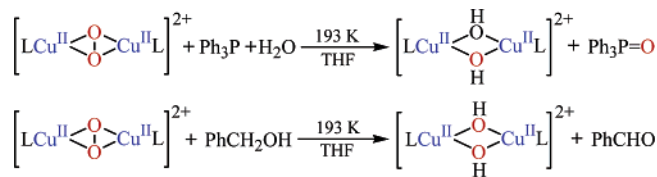


Figure 20. General reactivity of **2**: oxygen-atom transfer reagent (top) and 2H^+ , $2e^-$ oxidant (bottom).

distance is in line with other structurally characterized **P** complexes.^{37–39} Each Cu is best fit as a 5-coordinate center with four ligands at ca. 1.96 Å and an additional weakly associated ligand (Table 3). The latter distance is consistent with an oxygen or fluorine atom from a counteranion weakly associated in an axial position.¹⁷ Interestingly, the EXAFS fit for $2\cdot(\text{SbF}_6)_2$ allows ligands in the first coordination sphere to be differentiated into two groups, one with two scatterers at 1.85 Å and one with two scatterers at 1.99 Å (Figure 15, Table 3).⁴⁰ Overall, the variation of XAS, UV–vis, and rR spectra with counteranion suggests an intimate interaction of the counteranion with the metal center and thus an accessible Cu₂O₂ core (Table 2). The geometry-optimized DFT structure of the dication **2** (B3LYP/6-31G*) provides many insights into the structure of this complex. The calculated Cu–Cu, Cu–O and Cu–N distances correlate remarkably well with the solution EXAFS data for $2\cdot(\text{SbF}_6)_2$ for which the most detailed metric information is known (Figure 16).⁵⁴ The almost planar Cu₂O₂N₄ unit also supports the intense $\sim 244 \text{ cm}^{-1}$ Cu–N_{eq} rR stretch observed for this **P** complex.³⁵

The $2\cdot(\text{CF}_3\text{SO}_3)_2$ complex is very stable at 193 K ($t_{1/2} \approx 20$ days) given that DBED is a secondary diamine. This complex is thermally sensitive and decays in a first-order process at elevated temperatures, possibly through a ligand oxidation process, similar to other reported **P** complexes.¹⁴ The stability of $2\cdot(\text{CF}_3\text{SO}_3)_2$ allows the reactivity with exogenous substrates to be examined. The isomeric **P** and **O** species are thought to exhibit different reactivity with the former a better oxygen-atom transfer reagent⁵⁵ and the latter a better hydrogen-atom acceptor.²⁰ Consistent with these previous observations, $2\cdot(\text{CF}_3\text{SO}_3)_2$ reacts efficiently with PPh₃ at 193 K in THF to yield PPh₃O (>95% yield, >60% ¹⁸O incorporation) under pseudo-first-order conditions of PPh₃ (10 equiv), yet does not couple 2,4-di-*tert*-butylphenol to 3,3',5,5'-tetra-*tert*-butyl-2,2'-biphenol (Figure 18).⁵⁶ This lack of phenolic coupling supports an attenuated hydrogen-atom abstracting ability of $2\cdot(\text{CF}_3\text{SO}_3)_2$.²⁰ The reaction of $2\cdot(\text{CF}_3\text{SO}_3)_2$ with catechol, benzyl alcohol, and benzylamine gives good yields of quinone (95%), benzaldehyde (80%), and benzonitrile (70%), respectively, based on the oxidizing equivalents of **2**. The reactivity of a **P** species with the latter two substrates is unprecedented for such Cu/O₂ complexes.^{17,55,57} Generally, the **P** species can be construed both as an oxygen-atom transfer reagent and a mild 2H^+ , $2e^-$ oxidant (Figure 20).¹⁴

- (51) The high intensity of the 350 nm absorption band was confirmed by comparing oscillator strengths among several **P** species. The extinction coefficient multiplied by the width of half-height of the LMCT band for several **P** species (refs 23, 37, and 38) shows that the oscillator strength of **2** is up to 50% larger.
- (52) Henson, M. J.; Mukherjee, P.; Root, D. E.; Stack, T. D. P.; Solomon, E. I. *J. Am. Chem. Soc.* **1999**, *121*, 10332–10345.
- (53) Baldwin, M. J.; Root, D. E.; Pate, J. E.; Fujisawa, K.; Kitajima, N.; Solomon, E. I. *J. Am. Chem. Soc.* **1992**, *114*, 10421–10431.

- (54) Larger basis set geometry optimizations generally all lead to Cu–Cu distances in the vicinity of 3.6 Å, quite distinct from the experimental value.
- (55) Obias, H. V.; Lin, Y.; Murthy, N. N.; Pidcock, E.; Solomon, E. I.; Ralle, M.; Blackburn, N. J.; Neuhold, Y. M.; Zuberbühler, A. D.; Karlin, K. D. *J. Am. Chem. Soc.* **1998**, *120*, 12960–12961.
- (56) Many Cu/O₂ model complexes react with phenols to give the C–C coupled dimer of the phenol, which likely proceeds through a hydrogen-atom abstraction mechanism.
- (57) Except for one system (ref 17), no appreciable amounts of benzyl alcohol or benzylamine oxidation by other Cu/O₂ species has been reported.

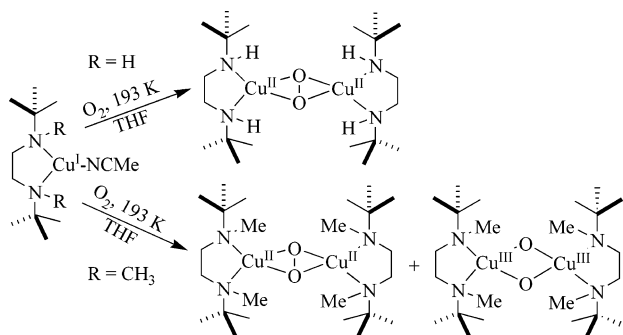


Figure 21. Differential reactivity toward O_2 of the Cu(I) complexes of two related diamine ligands, DBED (top) and DBDMED (bottom).

In contrast to the lack of phenol reactivity, $2 \cdot (CF_3SO_3)_2$ reacts rapidly with sodium or lithium salts of 2,4-di-*tert*-butylphenol at 193 K, and analysis of the products reveals an $\sim 1:1$ mixture of 3,5-di-*tert*-butylcatechol and 3,5-di-*tert*-butyl-1,2-benzoquinone as products. Assuming that the quinone product results from a rapid secondary oxidation of a catechol product by $2 \cdot (CF_3SO_3)_2$, $\sim 90\%$ of the oxidizing equivalents are used in this reaction. Alternatively, if the intermediacy of a semiquinone species is invoked, followed by its disproportionation into catechol in quinone products, the yield will be less. The use of $^{18}O_2$ in the formation of $2 \cdot (CF_3SO_3)_2$ followed by a reaction with phenolate clearly shows that a single oxygen atom is transferred to the catechol and quinone products, supporting direct oxygen-atom transfer to the phenolate substrate. This places $2 \cdot (CF_3SO_3)_2$ in a limited class of synthetic **P** species that efficiently hydroxylate phenolates, similar to tyrosinase.^{22,23,58}

4. Summary

DBED, a simple secondary diamine ligand, creates a remarkably stable **P** species with strong spectral and functional fidelity to that observed in oxyTyr and oxyHc. By contrast, the related tertiary diamine ligand DBDMED, which is more sterically demanding, forms a 50:50 ratio of **P** to **O** isomers under comparable conditions (Figure 21).^{18,59,60} While as little as a 2 kcal mol⁻¹ difference in free energy between the two systems could account for these observations at 193 K,²⁰ the similarity of these two chelating diamine ligands warrants some consideration about the attributes of DBED that lead to the formation of a **P** species.

At first glance, the secondary amines of DBED might be considered only as a less bulky analogue of the tertiary amines of DBDMED, yet gas phase acidity measurements clearly indicate that tertiary amines are more basic than their secondary amine counterparts. Thus, at parity of other factors, a tertiary amine is a stronger σ -donating ligand. Yet, this analysis excludes the greater steric demands of tertiary amines and their correspondingly lesser ability to interact with solvent or counterions, the latter of which can dominate the thermodynamic stability of a metal complex in an aqueous environment, as detailed by Clark et al.⁶¹ The higher energy Cu–N_{eq} vibrations for the **P**

species of DBDMED suggests stronger N–Cu(II) bonds. This stronger donation by DBDMED in its **P** species is also likely correlated to the greater relative stability of its **O** isomer, as a better σ -donor should be capable of stabilizing a higher oxidation state. Thus, we attribute the lesser σ -donation of the amines of DBED to its preferential stabilization of the Cu(II) centers in the **P** species, a situation much more in line with biological imidazole ligation.

5. Experimental Section

5.1. Materials and Methods. All solvents and reagents were obtained from commercial sources and used as received unless noted otherwise. THF, 2-methyltetrahydrofuran (MeTHF), and toluene (Aldrich) were distilled from sodium/benzophenone. CH_2Cl_2 was stirred over H_2SO_4 , washed with aqueous KOH followed by deionized water, and finally distilled from P_2O_5 in the absence of light. Acetone was refluxed (5 h) with anhydrous K_2CO_3 and distilled. All solvents were stored under a N_2 atmosphere. $[Cu(MeCN)_4](X)$ ($X = CF_3SO_3^-$, $CH_3SO_3^-$, SbF_6^- , BF_4^-) complexes were synthesized by a variation of literature methods.⁶² Preparation and manipulation of Cu(I) complexes were carried out in a N_2 drybox (Braun) with O_2 concentration < 1.0 ppm. *N,N'*-di-*tert*-butyl-ethylenediamine (DBED) was purchased from Aldrich, distilled in vacuo from CaH_2 , and stored under N_2 . The lithium or sodium salts of 2,4-di-*tert*-butylphenol were prepared according to a reported procedure.⁶³ Low-temperature UV–vis spectra were collected with a Polytec PI X-DAP-06 diode array spectrophotometer (190–820 nm) or a Cary 50 spectrophotometer (190–1100 nm) with a custom-designed immersible fiber-optic quartz probe with variable path length (1 and 10 mm; Hellma, Inc.). Constant temperatures were maintained either by a cooling bath (Kinetic Systems, New York) or a dry ice/acetone bath. The solution temperatures were monitored directly by insertion of an OMEGA temperature probe in the solutions. Solution 1H NMR and ^{13}C NMR measurements were performed on a Varian XL 400 MHz instrument using tetramethylsilane as the reference. X-band EPR spectra were collected on a Bruker EMX spectrometer with an ER041XG microwave bridge and ER4102ST cavity; samples were held in a liquid N_2 -filled finger Dewar.

The purity of the ligands and quantification of reaction products with Ph_3P , benzyl alcohol, benzylamine, 2,4-di-*tert*-butylcatechol, and 2,4-di-*tert*-butyl phenolate were assessed by GC–MS on an HP 5970 GC–MS equipped with an AT-5 (ALLTECH) column and mass selective detector, or on an HP 5890 GC equipped with a HP-DB1 column and FID detector, relative to an internal standard (mesitylene). Negative mode ESI-MS analysis $^{16}O/^{18}O$ -catechol products detection was performed on a Finnigan LCQ mass spectrometer.

5.2. Synthesis of $[(DBED)Cu(MeCN)](CF_3SO_3)$. Equimolar amounts of $[Cu(MeCN)_4](CF_3SO_3)$ (47 mg, 1.25 mmol) and DBED (21 mg, 1.25 mmol) were combined in 5 mL of THF in an inert atmosphere box to yield a 25 mM light yellow solution of $[(DBED)Cu(MeCN)](CF_3SO_3)$. As this solution turns yellow at RT over 48 h, it was generally used directly without isolation of the solid Cu(I) complex. 1H NMR (CD_2Cl_2 , 400 MHz): δ 1.20 (s, 18H, *t*Bu), 2.05 (s, 12H, MeCN), 2.69 (s, 4H, CH_2). X-ray crystallography information is provided.³⁴

5.3. Synthesis of $[(DBED)_2Cu_2(\mu-OH)_2] \cdot (X)_2$ ($X = CF_3SO_3^-$ or BF_4^-). Equimolar amounts of DBED and $[Cu(MeCN)_4](X)$ ($X = CF_3SO_3^-$ or BF_4^-) were mixed in THF (20 mM) and exposed to air at RT to give a blue solution of $[(DBED)_2Cu_2(\mu-OH)_2] \cdot (X)_2$ ($3 \cdot (X)_2$). Green-blue needles suitable for X-ray diffraction were obtained by slow vapor diffusion of pentane into 1:1 THF/ CH_2Cl_2 solutions of $[(DBED)_2Cu_2(\mu-OH)_2](BF_4)_2$ at RT. A metrically similar X-ray structure of the

(58) The equilibrium mixture of **P** and **O** species formed with DBDMED does not hydroxylate phenolates in appreciable yields.

(59) Liang, H.-C.; Zhang, C. X.; Henson, M. J.; Sommer, R. D.; Hatwell, K. R.; Kaderli, S.; Zuberbühler, A. D.; Rheingold, A. L.; Solomon, E. I.; Karlin, K. D. *J. Am. Chem. Soc.* **2002**, *124*, 4170–4171.

(60) Taki, M.; Teramae, S.; Nagatomo, S.; Tachi, Y.; Kitagawa, T.; Itoh, S.; Fukuzumi, S. *J. Am. Chem. Soc.* **2002**, *124*, 6367–6377.

(61) Clark, T.; Hennemann, M.; van Eldik, R.; Meyerstein, D. *Inorg. Chem.* **2002**, *41*, 2927–2935.

(62) Kubas, G. J.; Monzyk, B.; Crumbliss, A. L. *Inorg. Synth.* **1979**, *19*, 90–92.

(63) Mandal, S.; Macikenas, D.; Protasiewicz, J. D.; Sayre, L. M. *J. Org. Chem.* **2000**, *65*, 4804–4809.

dication of lower resolution was obtained for $3 \cdot (\text{CF}_3\text{SO}_3)_2$. Elemental analysis for $\text{C}_{20}\text{H}_{50}\text{B}_2\text{Cu}_2\text{F}_8\text{N}_4\text{O}_2$ ($3 \cdot (\text{BF}_4)_2$), calcd (found) %: C 35.36 (35.07), H 7.42 (7.55), N 8.25 (8.00). All other characterizations were performed only for $3 \cdot (\text{CF}_3\text{SO}_3)_2$. Elemental analysis for $\text{C}_{22}\text{H}_{50}\text{Cu}_2\text{F}_6\text{N}_4\text{O}_8\text{S}_2$ ($3 \cdot (\text{CF}_3\text{SO}_3)_2$), calcd (found) %: C 32.87 (32.56), H 6.27 (6.34), N 6.97 (6.77). ESI-MS: 804.9 ($3 \cdot (\text{CF}_3\text{SO}_3)_2 + \text{H}^+$). IR (KBr): $\nu = 3433$ (O–H), 3197 (N–H), 2979 (C–H), 1378, 1251, 1165, 1033, 641 (CF_3SO_3) cm^{-1} . UV–vis (λ_{max} (ϵ , $\text{M}^{-1} \text{cm}^{-1}$), THF): 273 (8000), 328 (sh), 360 (sh), 675 nm (240). ^1H NMR (THF- d_6): $\delta = 1.25$ (s, 9H), 1.28 (s, 18H), 1.38 (s, 9H), 2.94 (m, 4H). X-ray crystallography information is provided.³⁴

Solid-state magnetic susceptibility measurements of ground samples of $2 \cdot (\text{CF}_3\text{SO}_3)_2$ were collected using a Quantum Design MPMS2 SQUID magnetometer from 5 to 300 K for two different samples. Experimental susceptibility data were corrected for diamagnetic contributions and for temperature-independent paramagnetism ($N_{\alpha} = 60 \times 10^{-6} \text{ cm}^3 \text{ mol}^{-1}$ per Cu center), and the $-2J$ convention was applied.

5.4. Synthesis of [(DBED)₂Cu₂(O₂)](X)₂. A 0.5 mM solution of [(DBED)₂Cu₂(O₂)](X)₂ was prepared by injecting a 200 μL solution of [(DBED)Cu(MeCN)](X) (25 mM, THF) into a precooled (193 K), O₂ (1 atm) saturated solution (5 mL) of CH₂Cl₂, acetone, THF, MeTHF, or toluene. The following data is for [(DBED)₂Cu₂(O₂)](CF₃SO₃)₂. ^1H NMR (CD₂Cl₂, 193 K, 400 MHz): δ 1.18 (s, 36H, *t*Bu), 2.05 (s, 24H, MeCN), 2.61 (s, 4H), 2.67 (s, 4H). UV–vis (λ_{max} (ϵ , $\text{M}^{-1} \text{cm}^{-1}$), THF): 350 (36 000), 485 (1200), 605 nm (900). EPR (77 K, MeTHF): silent.

5.5. Beer's Law Plot. Solutions of varying concentrations of $2 \cdot (\text{CF}_3\text{SO}_3)_2$ (0.03–0.8 mM) in THF were obtained by chilling the solutions of $1 \cdot \text{CF}_3\text{SO}_3$ to 193 K in a dry ice/acetone bath and adding O₂ by bubbling with a fine needle, whereupon the solution turned green. The absorption band at 350 nm was monitored with either a 1 or 0.1 cm path length probe. The slope of the absorbance versus $2 \cdot (\text{CF}_3\text{SO}_3)_2$ concentration gives an extinction coefficient of ca. 36 000 $\text{M}^{-1} \text{cm}^{-1}$. The $\sim 10\%$ THF contraction from 298 to 193 K was not applied to the extinction coefficient calculation.

5.6. Spectrophotometric Titration. A 20 mL solution of $1 \cdot \text{CF}_3\text{SO}_3$ in THF (1 mM) was cooled to 193 K in a dry ice/acetone bath, and aliquots of dry pure O₂ were injected into the reaction flask via a 250 μL gastight syringe. The stirred solution was left to equilibrate as assessed through the absorbance at 350 nm. Repeated runs (four) gave a Cu/O₂ ratio of 2:1.1(1).

5.7. Formation Kinetics. The kinetics of formation were monitored through the characteristic optical bands at ~ 350 nm at 193 K. Formation of $2 \cdot (\text{CF}_3\text{SO}_3)_2$ was achieved by injecting a concentrated solution of $1 \cdot \text{CF}_3\text{SO}_3$ in a precooled THF solution saturated with a 2% atm O₂/N₂ gas mixture ([Cu] = 0.033 mM, [O₂] = 0.3 mM, THF). For each run a multiwavelength component analysis (250–450 nm) was performed using SPECFIT (Spectrum Software Associates) to obtain rate constants. Good first-order A \rightarrow B fits were obtained.

5.8. X-ray Absorption Spectroscopy. **5.8.1. Sample Preparation.** A THF or MeTHF solution of [(DBED)Cu^{II}]₂(O₂)](X)₂ ($2 \cdot \text{X}_2$, X = CF₃SO₃[−], CH₃SO₃[−], SbF₆[−]) ([Cu] = 1.8 mM) was prepared by stirring a sample of [(DBED)Cu^I(MeCN)](X) ($1 \cdot \text{X}$) under 1 atm of O₂ for 30 min at 193 K. A precooled Lucite sample cell with a Kapton tape window ($\sim 120 \mu\text{L}$) was filled by immersion into the solution of $2 \cdot \text{X}_2$ at 193 K. The filled cell was rapidly removed and immediately frozen in liquid N₂ and maintained at this or lower temperatures throughout the experiment.

5.8.2. Data Collection and Analysis. The Cu K-edge X-ray absorption spectrum was measured at the Stanford Synchrotron Radiation Laboratory (SSRL) on unfocused 8-pole wiggler beam line 7-3, with the ring operating at 3 GeV, 50–100 mA. A Si(220) monochromator was used for energy selection. The monochromator was detuned 50% at 9868 eV to minimize higher harmonic components in the X-ray beam. The sample was maintained at 10 K during data

collection using an Oxford Instruments CF1208 continuous flow liquid helium cryostat. Data were measured in fluorescence mode using a Canberra Ge 30-element array detector. XAS data were measured to $k = 15 \text{ \AA}^{-1}$. Internal energy calibration was performed by simultaneous measurement of the absorption of a Cu foil placed between two ionization chambers located after the sample. The first inflection point of the foil was assigned to 8980.3 eV. As no photoreduction was observed during the collection of the data, all scans collected were averaged. Averages included 12 scans for $2 \cdot (\text{CF}_3\text{SO}_3)_2$, 16 scans for $2 \cdot (\text{CH}_3\text{SO}_3)_2$, and 20 scans for $2 \cdot (\text{SbF}_6)_2$.

The averaged data were processed by fitting a second-order polynomial to the postedge region and subtracting this background from the entire spectrum. A three-region spline of orders 2, 3, and 3 was used to model the smooth background above the edge. The resultant EXAFS was k^3 -weighted to enhance the impact of high- k data. Because of zinc contamination (the Zn K-edge is at $k = 13.4 \text{ \AA}^{-1}$) in the sample, the EXAFS data were truncated at $k = 12.5 \text{ \AA}^{-1}$ for the analyses.

Theoretical EXAFS signals $\chi(k)$ were calculated using FEFF (version 6.0)⁶⁴ and fit to the data using EXAFSPAK.⁶⁵ The experimental energy threshold, E_0 (the point at which $k = 0$), was chosen as 9000 eV. The structural parameters that were varied during the refinements include the bond distance (R) and the bond variance (σ^2). The σ^2 is related to the Debye–Waller factor that is a measure of thermal vibration and static disorder of the absorbers and scatterers. Coordination numbers were systematically varied during the course of the analysis but were not allowed to vary within a given fit.

5.9. Resonance Raman Spectroscopy. Laser excitation lines of 351.1, 379.5, 457.9, and 496.5 nm (provided by a Coherent Innova Sabre 25/7 Ar⁺ CW ion laser) were chosen to enhance and probe the copper–oxygen modes. Resonance Raman spectra were obtained using a Princeton Instruments ST-135 back-illuminated CCD detector on a Spex 1877 CP triple monochromator with a 2400 grooves/mm (351.1 and 379.5 nm) or 1200 grooves/mm (457.9 and 496.5 nm) holographic spectrograph grating. Spectral resolution was $< 2 \text{ cm}^{-1}$. Sample spectra were collected at ~ 77 K with a liquid N₂-filled finger Dewar. Isotopic substitution was achieved by oxygenation with ¹⁸O₂ (Icon, 99%).

5.10. Computational Details. Broken symmetry geometry optimizations were performed using the Gaussian 98/03 programs, with the unrestricted B3LYP hybrid functional and a 6-31G* basis set.³⁴

5.11. Thermal Decomposition Studies. The kinetics of decomposition of $2 \cdot (\text{CF}_3\text{SO}_3)_2$ were studied by monitoring the decay of the characteristic optical bands at various temperatures (193–273 K); constant temperatures were maintained by a cooling bath (Kinetic Systems, New York). Approximately 2 min was required for temperature equilibration within the reaction solution starting from 193 K and warming to the desired temperature, which was monitored internally with an OMEGA temperature probe. Only data after thermal equilibration were used for determining rate constants. A multiwavelength component analysis (250–450 nm) was performed with SPECFIT to obtain rate constants; the number of significant eigenvectors obtained was generally 2 for all data sets. Good first-order (A \rightarrow B) fits were obtained for all data sets.

5.12. Ligand Oxidation Analysis. To the thermally decomposed solution of $2 \cdot (\text{CF}_3\text{SO}_3)_2$ in THF at 233 K, aqueous ammonia (30%) was added at RT dropwise until the THF layer turned colorless. The organic layer was passed through a column of neutral activated alumina (Brockmann I, ~ 150 mesh, 58 \AA) followed by the aqueous layer. The blue copper product was retained on the column while the ligand products eluted. The column was carefully washed with MeOH (2 mL), and the combined solutions were dried over K₂CO₃. The solution was concentrated to ~ 2 mL, and a stoichiometric amount of tetraethyleth-

(64) Rehr, J. J.; Mustre de Leon, J.; Zabinsky, S. I.; Albers, R. C. *J. Am. Chem. Soc.* **1991**, *113*, 5135–5140.

(65) George, G. N. *EXAFSPAK & EDG_FIT*; Stanford Synchrotron Radiation Laboratory, Stanford Linear Accelerator Center; Stanford University: Stanford, CA, 2000.

ylenediamine or mesitylene was added as an internal calibrant. The ligand products were subjected to GC/GC–MS analysis. Control experiments without any copper were performed to calibrate the workup procedure relative to the added internal standard. Approximately 80% of the original ligand was recovered, and no decomposition product was formed in more than 10% yield. Analysis of DBED: GC–MS [50 °C (5 min) at 20 °C/min to 250 °C (5 min)]; $t_r = 9.5$ min (172, M⁺). ¹H NMR (CD₂Cl₂, 400 MHz): δ 1.12 (s, 18H, *t*Bu), 2.67 (s, 4H, CH₂), 3.40 (s, 2H, NH).

5.12.1. Preparation of *d*₂-DBED. DBED was dissolved in dry THF and excess D₂O (99.9%, Icon Isotopes) was added. The solvent was removed under vacuum, and the residue was redissolved in dry THF and excess D₂O. After several washings with D₂O, the solution was dried over K₂CO₃ and solvent removed to obtain *N,N'*-*d*₂-DBED (>95% D by GC–MS and ¹H NMR). Neither the formation rate nor thermal decay rate of the 2•(CF₃SO₃)₂ was impacted with the deuterated ligand ($k_H/k_D = 1 \pm 0.1$).

5.13. Oxidation of Exogenous Substrates. A solution of 2•(CF₃SO₃)₂ (5 mM, 5 mL) in THF (N₂ atmosphere, 193 K) was prepared from 1•CF₃SO₃ and excess O₂. For anaerobic reactions, the excess O₂ was removed prior to addition of substrates by purging with N₂ for 15 min. For the benzyl alcohol and benzylamine substrates, 2 equiv were added, and solutions were stirred at 233 K for 12 h. All other substrates reacted readily at 193 K under N₂. The resulting solutions were passed through a column of neutral activated alumina (Brockmann I, ~150 mesh, 58 Å) followed by 2 column volumes of MeOH. The copper product was retained, while the organic products eluted. The reaction mixtures were subjected to GC/GC–MS analysis. Mass recovery of the products was always >90% as deduced by addition of internal calibrants benzonitrile and acetophenone for alcohols and amines, respectively.

The reaction of 2,4-di-*tert*-butylphenolate was performed at 193 K in THF with excess O₂ removed. Addition of 1 equiv of substrate (0.05 mL, 50 mM solution in THF) changed the color from dark green to light yellow-green. After 15 min, the reaction was quenched with H₂-

SO₄ (0.5 M, 2 mL), and the solvent was removed. The residue was extracted with chloroform and analyzed by ¹H NMR and GC–MS. The amounts of phenol, catechol, and quinone were quantified by comparing with known mixtures of pure compounds. For ¹⁸O-2•(CF₃SO₃)₂, the residue was analyzed by negative mode ESI-MS to determine the ratio of ¹⁶O/¹⁸O products, revealing more than 80% ¹⁸O incorporation.

Acknowledgment. We thank Dr. Viswanath Mahadevan and Dr. Xavier Ottenwaelder for experimental assistance and helpful discussions. L.M.M. gratefully acknowledges a John Stauffer Stanford Graduate Fellowship and a Franklin Veatch Memorial Fellowship. Funding was provided by NIH GM50730 (T.D.P.S), NIH RR01209 (K.O.H.), and NIH DK31450 (E.I.S.). XAS data were measured at SSRL that is supported by the Department of Energy, Office of Basic Energy Sciences. The SSRL Structural Molecular Biology program is funded by the National Institutes of Health, National Center for Research Resources, Biomedical Technology Program, and the Department of Energy, Office of Biological and Environmental Research.

Supporting Information Available: Experimental details including syntheses of all ligands, Cu(I) complexes, and bis-(μ -hydroxo)dicopper(II) complexes; initial rates plot for the oxygenation of Cu(I) complexes; Eyring plots and kinetic data for thermal decomposition of 2•(CF₃SO₃)₂; description of UV–vis, resonance Raman, and XAS experiments, kinetic measurements, CIF files for the crystal structures of 2•CF₃SO₃ and 3•(BF₄)₂, and Cartesian coordinates for the geometry-optimized structure of 2 (14 pages, print/PDF). This material is available free of charge via the Internet at <http://pubs.acs.org>.

JA056740V